Electronic Supplementary Material (ESI) for Energy & Environmental Science.
This journal is © The Royal Society of Chemistry 2024

Supplementary Information

Silicon nanowire/ionic hydrogel-based hybrid moist-electric generators with enhanced voltage output and operational stability

Wenjing Duan,[a,c#] Beibei Shao,[b,c#] Zhiqi Wang,[a,c] Kun Ni,[a,c] Shanfei Liu,[a,c] Xianrong Yuan,[b,c] Yusheng Wang,[b,c] Baoquan Sun,[b,c] Xiaohong Zhang,[b,c] Ruiyuan Liu[a,c]*

[a]Soochow Institute of Energy and Material Innovations, Key Laboratory for Advanced Carbon Materials and Wearable Energy Technologies of Jiangsu Province, College of Energy, Soochow University, Suzhou, 215006, Jiangsu, PR China.

[b]Institute of Functional Nano & Soft Materials (FUNSOM), Soochow University, Suzhou, 215123, Jiangsu, PR China.

[c]Jiangsu Key Laboratory of Advanced Negative Carbon Technologies, Soochow University, Suzhou, 215123, Jiangsu, PR China.

* Correspondence should be addressed to: ryliu@suda.edu.cn

[#] These authors contributed equally to this work.

Table of Contents

Numerical Simulation

The concentration distribution of ions and surface charge density distribution were both numerically calculated by using the commercial finite−element software package COMSOL (version 5.6) Multiphysics based on the built−in coupled two−dimensional Nernst−Planck−Poisson (PNP) equations. The model is simplified by assuming steady−state conditions, and considering the modeling and computational complexity of three−dimensional models, a 2D model is adopted. The numerical simulation model based on the 2D structure is shown in Fig. SI. Simplified nano−channels were realized by constructing a gap between two nanowires (the channel surface is dominantly negative and the length is 10 μm).

The PNP equations are recalled below[1, 2]:

The Nernst−Planck equation describes the fluxes of mobile ions and transport properties of a charged nanochannel:

$$j_i = D_i\left(\nabla c_i + \frac{z_i F c_i}{RT}\nabla\varphi\right) \tag{1}$$

The Poisson equation defines the relationship between the electrical potential and ion concentrations:

$$\nabla^2\varphi = -\frac{F}{\varepsilon}\sum z_i c_i \tag{2}$$

When the system reaches a stationary regime, the flux must satisfy the following equation:

$$\nabla \cdot j_i = 0 \tag{3}$$

Above, j_i, D_i, c_i, z_i, φ, ε, F, R, and T are, respectively, the ionic flux, diffusion coefficient, ion concentration, valence number for each species i, electrical potential, dielectric constant of the solution, Faraday constant, universal gas constant, and absolute temperature.

The ion flux has the zero normal components at boundaries:

$$n \cdot j_i = 0 \tag{4}$$

The boundary condition for the potential φ on the channel walls is:

$$n \cdot \nabla\varphi = -\frac{\sigma}{\varepsilon} \tag{5}$$

where σ represents the surface charge density. The formation of the electric field is considered as being due to the different surface charge densities of the heterostructure. Therefore, the surface charge density of the SiNWs is set to be $-2e^{-6}$ C m^{-2}. If the inorganic salt is LiCl, the initial concentrations of the mobile ions Li^+ and Cl^- in the left reservoir are both set to 1×10^{-10} mol L^{-1}, and the initial concentrations of the mobile ions in the right reservoir are both set to 1×10^{-7} mol L^{-1}. If the inorganic salt is $CaCl_2$, the initial concentrations of the mobile ions Ca^{2+} and Cl^- in the left reservoir are set to 1×10^{-10} mol L^{-1} and 2×10^{-10} mol L^{-1}, and the initial concentrations of the mobile ions in the right reservoir are set to 1×10^{-7} mol L^{-1} and 2×10^{-7} mol L−1, respectively, and the initial concentrations of mobile ions in the right reservoir are set to 1×10^{-7} mol $L^{-1}$and 2×10^{-7} mol L^{-1}, respectively. If the inorganic salt is $AlCl_3$, the initial concentrations of mobile ions $Al^{3+}$and Cl^- in the left reservoir are set to 1×10^{-10} mol $L^{-1}$and 3×10^{-10} mol L^{-1}, respectively. The initial concentrations of mobile ions in the right reservoir are set to 1×10^{-7} mol $L^{-1}$and 3×10^{-7} mol L^{-1}, respectively. The surface charge density of water reservoir is set to 0 C m^{-2}. With the given geometry and suitable boundary conditions, the coupled PNP equations are solved with finite−element calculations for the ion concentration distribution.

Table S1 | BET surface area and pore parameters of composite layers loaded with different masses of hydrogels.

Hydrogels weight (mg)	BET surface area (m^2 g^{-1})	Pore diameter (nm)
40	4.60	22.45
60	3.08	20.31
80	2.97	17.68
100	0.63	16.14
220	0.31	/

Table S2 | Comparison of different materials for MEGs.

Functional material	Voltage (V)	Operational time (h)	Reference
Porous carbon films	0.068	12	3
Porous GO membrane	0.45	100	4
Waste corn stalk	0.6	40	5
E-spun cellulose acetate	0.3	50	6
Biological nanofibrils	0.1	10	7
Electrolyte-loaded nanofiber	0.7	120	8
Ionic hydrogel and carbon	0.65	170	9
GO film	0.02	Intermittent	10
GO/PAAS	0.6	120	11
Ppy nanowire	0.072	Intermittent	12
Ppy nanoarray	0.15	Intermittent	13
PAM-LiCl hydrogels/SiNWs	**1.28**	**800 (60%)**	**This work**

Table S3 | Comparison of reported organic-inorganic hydrovoltaic devices.

Functional material	Mechanism	Voltage (V)	Operational time (h)	Reference
GO/PAAS	Moisture	0.6	120 h	11
PA-CPDs	Moisture	0.8	1800 s	14

SA-SiO_2-rGO	Moisture adsorption-desorption	0.5	12000 s	15
PNCs-SiNWs	Evaporation	0.45	500 s	16
PEDOT-GO	Evaporation-Moisture	0.49	250 m	17
Ionic hydrogel-carbon	Moisture	0.65	170 h	9
Carbon fabric-PEDOT:PSS/PAM-LiCl hydrogels/SiNWs/Ag	**Moisture**	**1.28**	**800 h (60%)**	**This work**

Table S4 | Comparison of reported silicon-based hydrovoltaic devices.

Device structure	Mechanism	Voltage (V)	Operational time	Reference
C/SiNWs/Ag	Evaporation	0.4	350 s	18
PNCSi-HD	Evaporation	0.45	500 s	16
Fabric electrode/SiNWs/Ag	Evaporation	0.55	15 h	19
Fabric electrode/SiNWs/TiO_2/Ag	Evaporation	0.82	200 s	20
CNT/PDDA/SiNWs/Ag	Moisture	1.0	75 h	21
CNT/P(VDF-TrFE)/SiNWs/Ag	Evaporation	1.04	16 h	22
Carbon fabric-PEDOT:PSS/PAM-LiCl hydrogels/SiNWs/Ag	**Moisture**	**1.28**	**800 h (60%)**	**This work**

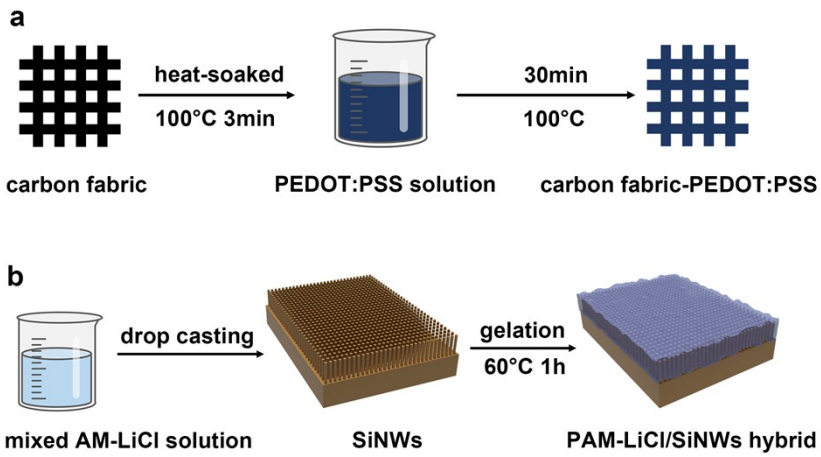

Figure S1 | Schematic illustration of the fabrication process of the CFP and PAM-LiCl ionic hydrogels/SiNWs hybrid. (a) Preparation of highly conductive CFP by heat-soaked of CF in PEDOT:PSS. (b) PAM-LiCl ionic hydrogels/SiNWs hybrid was prepared by drop-casting a mixed AM-LiCl solution on SiNWs after gelation at a certain temperature.

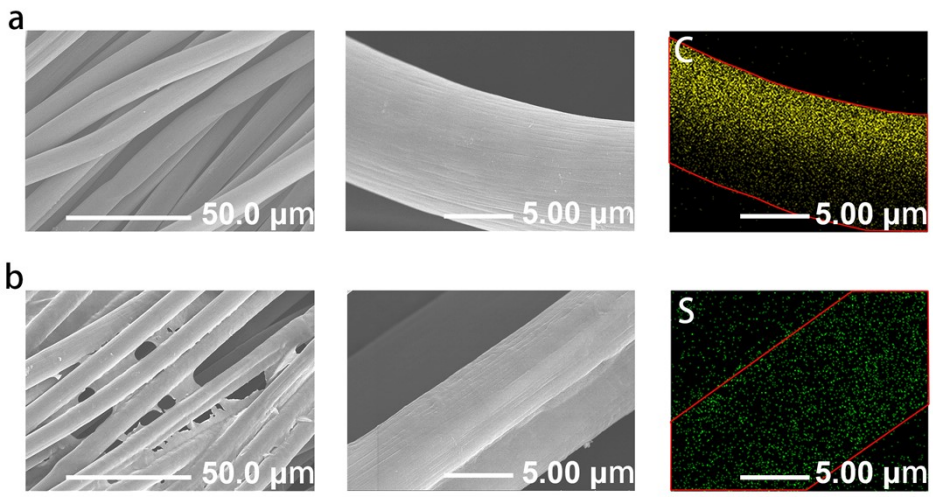

Figure S2 | Top-view SEM and EDS images of the (a) CF and (b) CFP.

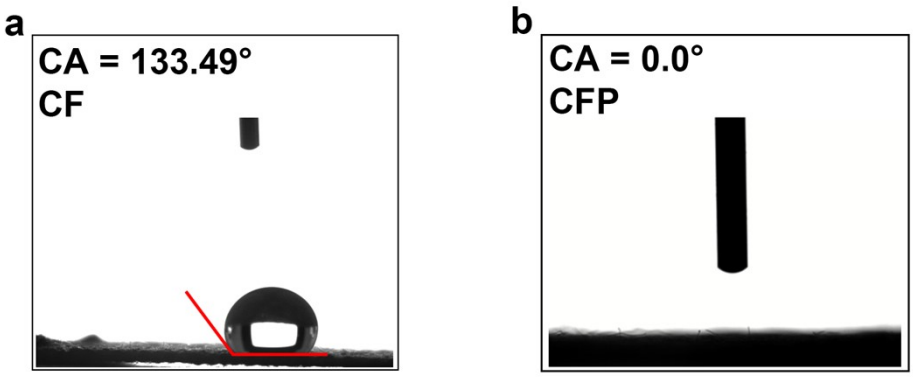

Figure S3 | The contact angle of CF and CFP. (a) The contact angle of CF is 133.49°, which indicates its hydrophobicity. (b) The contact angle of CFP is 0.0°, which indicates its hydrophilicity.

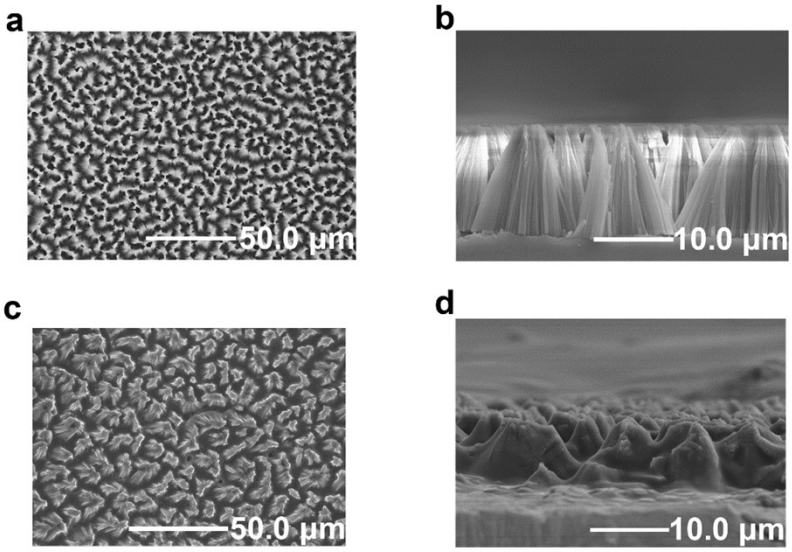

Figure S4 | The SEM image of SiNWs and PAM-LiCl ionic hydrogels/SiNWs hybrid. PAM-LiCl ionic hydrogels encapsulates SiNWs. SiNWs still exhibits its original shape, and PAM-LiCl ionic hydrogels retains its porosity. (a) Top-view SEM image of SiNWs. (b) Cross-section SEM image of SiNWs. (c) Top-view SEM image of PAM-LiCl ionic hydrogels/SiNWs hybrid. (d) Cross-section SEM image of PAM-LiCl ionic hydrogels/SiNWs hybrid.

Figure S5 | The contact angle of PAM-LiCl ionic hydrogels/SiNWs hybrid (PAM-LiCl ionic hydrogels 100 mg).

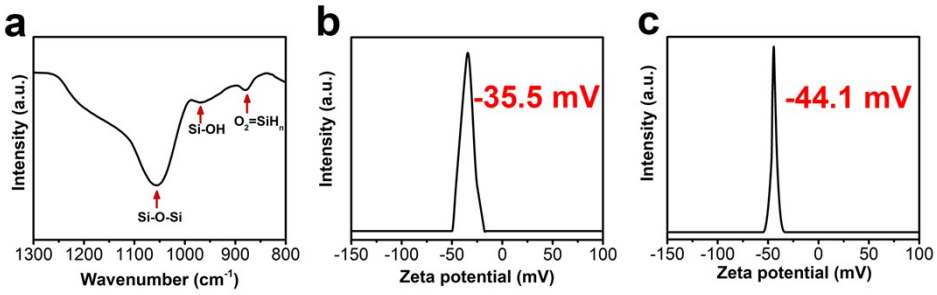

Figure S6 | The characteristics of SiNWs and PAM/SiNWs hybrid. (a) FTIR spectrum of SiNWs. (b) Zeta potential of SiNWs and (c) PAM/SiNWs hybrid.

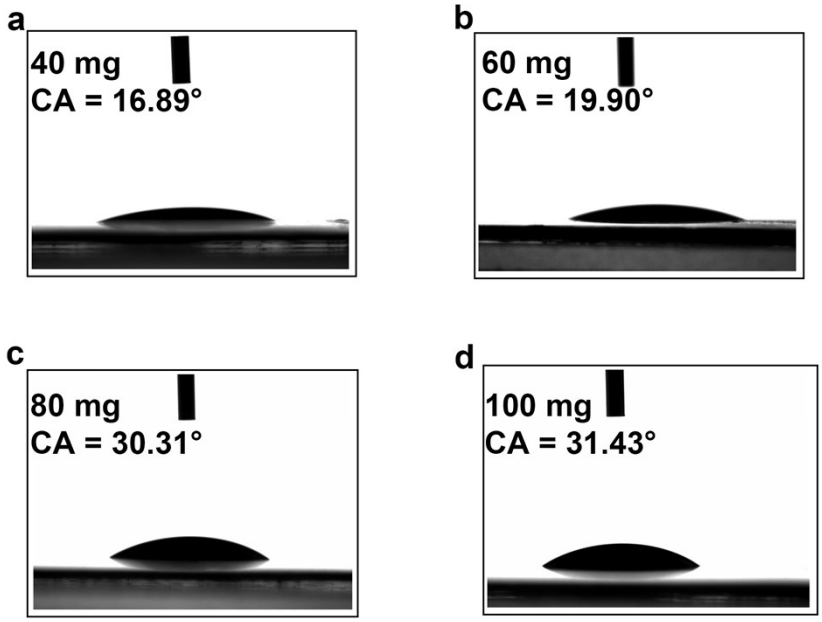

Figure S7 | The contact angles of SiNWs loaded with different weight of PAM-LiCl ionic hydrogels. As the weight of the PAM-LiCl ionic hydrogels increases, the hydrophilicity of the hybrids decreases. When the weight of the load PAM-LiCl ionic hydrogels is (a) 40 mg, (b) 60 mg, (c) 80 mg and (d) 100 mg, the contact angles are 16.89°, 19.90°, 30.31° and 31.43° respectively.

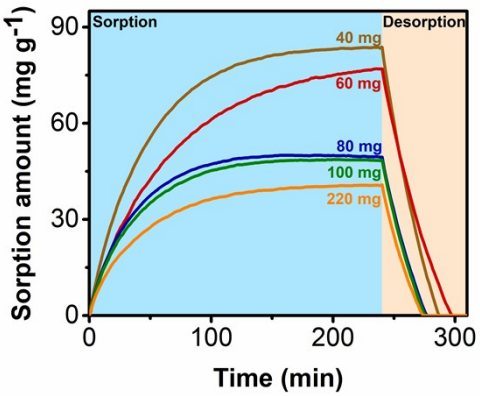

Figure S8 | DVS curves show the dynamic water absorption-desorption process of hybrid layers loaded with different masses of hydrogels at 35 °C and 60% *RH*. As the weight of the PAM-LiCl ionic hydrogels increases, the sorption amount of the hydrogels gradually decreased when the weight of the PAM-LiCl ionic hydrogel was (a) 40 mg, (b) 60 mg, (c) 80 mg, (d) 100 mg and (e) 220 mg.

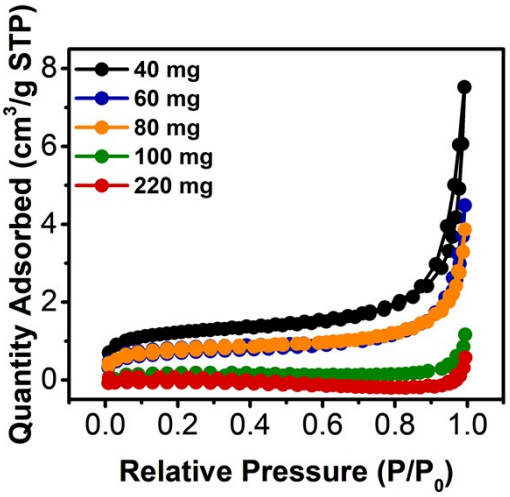

Figure S9 | Nitrogen adsorption-desorption isotherms of hybridized layers loaded with different masses of hydrogels.

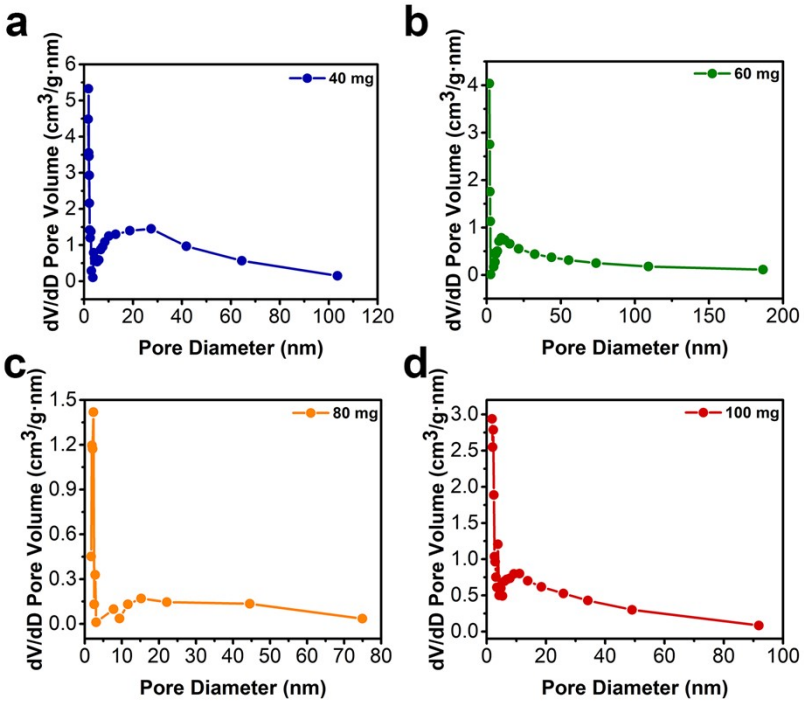

Figure S10 | Pore size distribution of hybridized layers loaded with different masses of hydrogels.

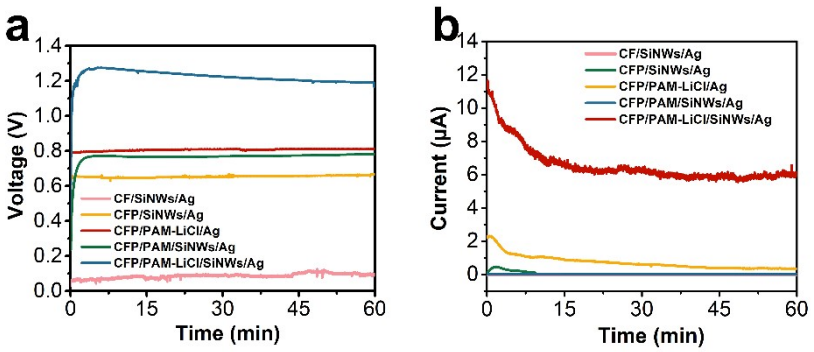

Figure S11 | (a) Voltage and (b) current of MEGs with different structures (PAM-LiCl ionic or PAM hydrogels 100 mg, 35 °C and 60% *RH*).

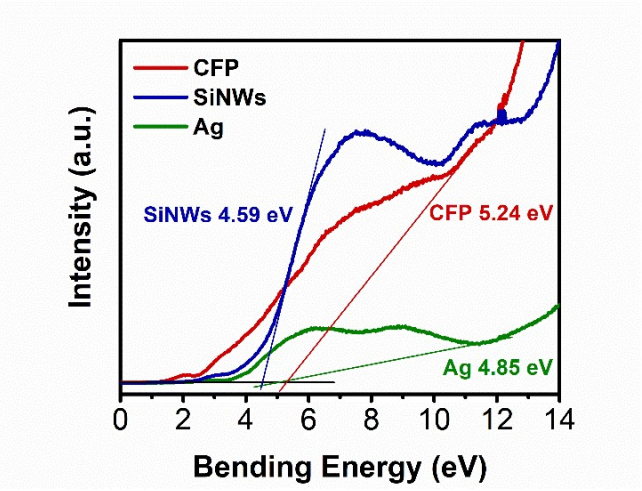

Figure S12 | UPS measurements of CFP, SiNWs and Ag with work function values of approximately 5.24 eV, 4.59 eV, and 4.85 eV, respectively.

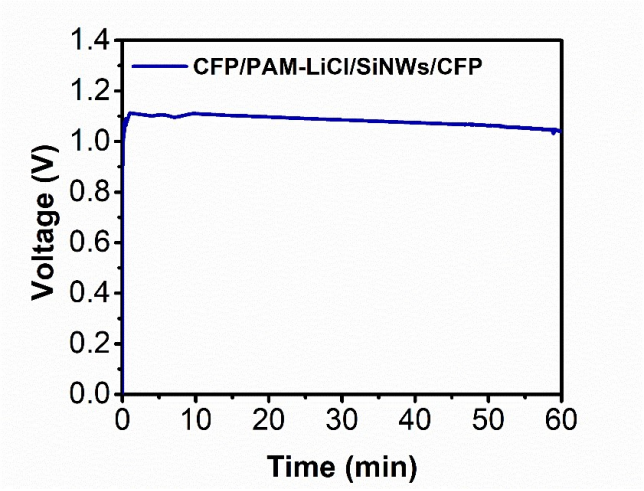

Figure S13 | Output voltage for the MEG with CFP/PAM-LiCl/SiNWs/CFP (PAM-LiCl ionic hydrogels 100 mg, 35 °C and 60% *RH*).

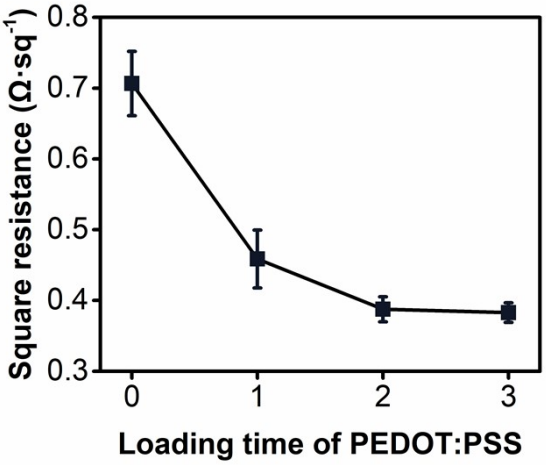

Figure S14 | Square resistance of PEDOT:PSS-coated carbon fabric with different PEDOT:PSS loading times.

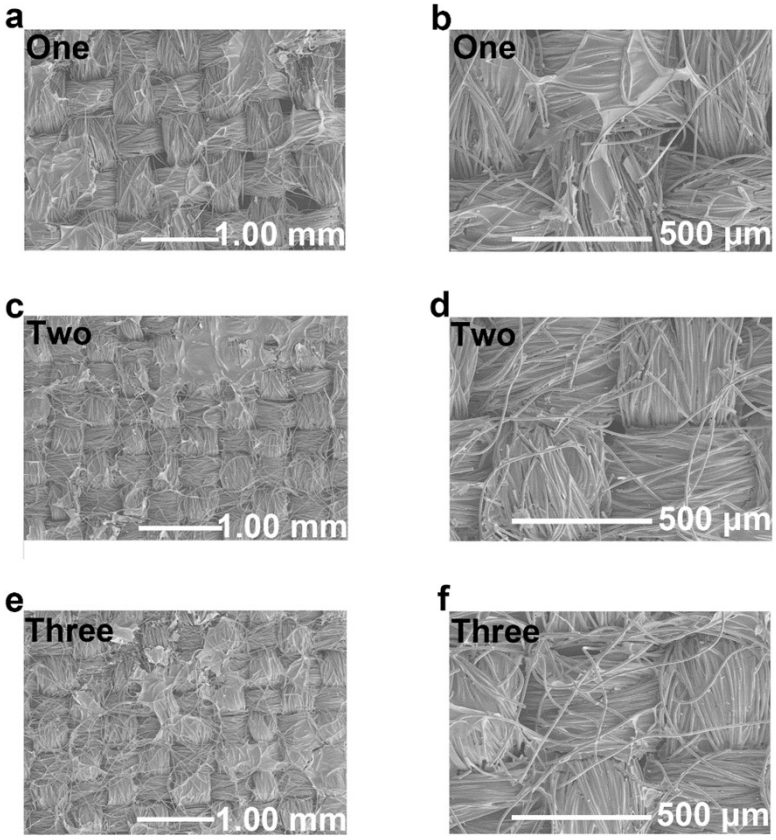

Figure S15 | The SEM image of carbon fabrics soaked with PEDOT:PSS for different times. (a) and (b) The SEM image of carbon fabric soaked in PEDOT:PSS for one time. (c) and (d) The SEM image of carbon fabric soaked in PEDOT:PSS for twice. (e) and (f) The SEM image of carbon fabric soaked in PEDOT:PSS for three times.

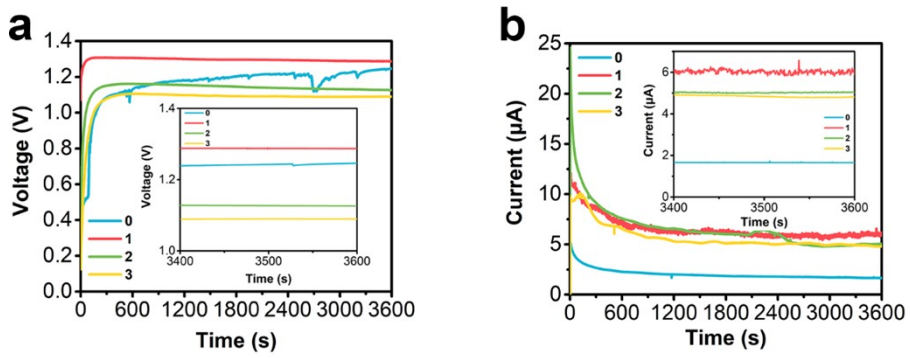

Figure S16 | (a) Voltage and (b) current of the MEGs by using carbon fabrics heat-soaked in PEDOT:PSS for different times (PAM-LiCl ionic hydrogels 100 mg, 35 °C and 60% *RH*).

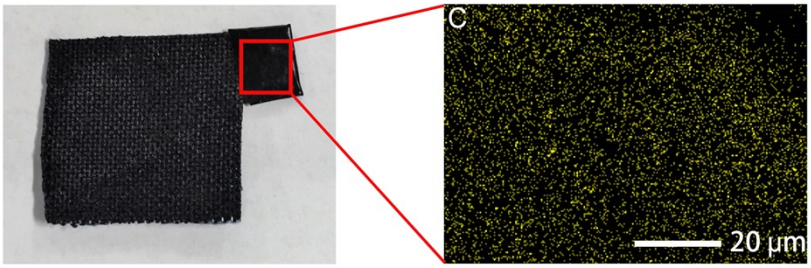

Figure S17 | The optical image of CFP wrapped with conductive carbon tape and the EDS image of carbon tape.

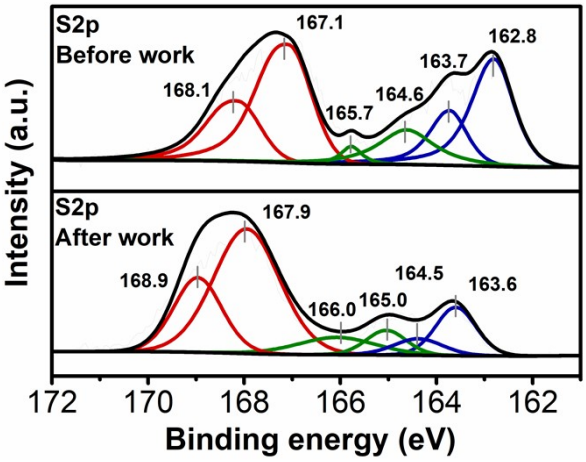

Figure S18 | XPS showing variations in the S element of the upper electrode before and after operation. The S element did not undergo a valence change, indicating that the upper electrode was not involved in the reaction.

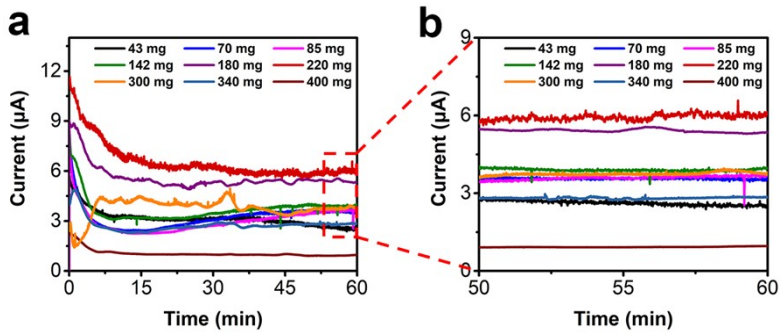

Figure S19 | Current of MEGs by drop casting PAM-LiCl ionic hydrogels of different weights for (a) 0 min to 60 min and (b) 50 min to 60 min (35 °C and 60% *RH*).

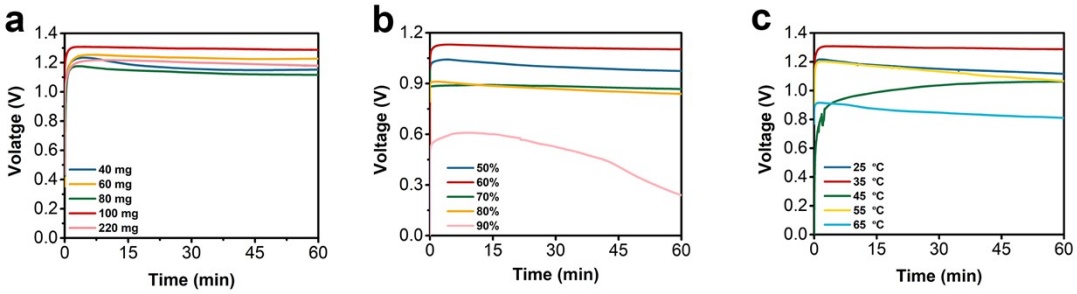

Figure S20 | Voltage output of MEG under different conditions (loaded ionic hydrogel weights, temperatures and humidities). Voltage outputs of MEGs (a) with different weights of PAM-LiCl ionic hydrogels (35 °C and 60% *RH*), (b) at different *RH*s (PAM-LiCl ionic hydrogels 100 mg and 35 °C), and (c) at different temperatures (PAM-LiCl ionic hydrogels 100 mg and 60% *RH*).

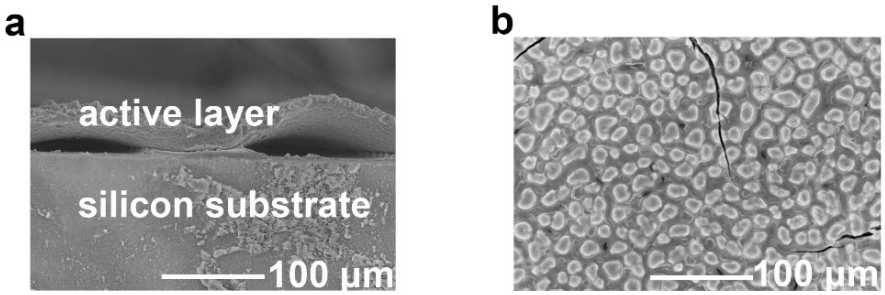

Figure S21 | The SEM image of the ionic hydrogels before and after working for 800 hours. Prolonged exposure to high temperature and excessive humidity will cause swelling of the PAM-LiCl ionic hydrogels in the hybrid, resulting in cracking and detachment from the silicon substrate. (a) Top-view and (b) cross-section SEM image of PAM-LiCl ionic hydrogels/SiNWs hybrid.

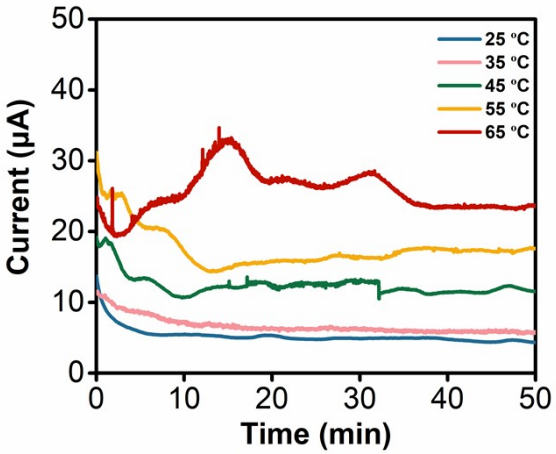

Figure S22 | Current outputs of the hybrid MEG at different temperatures (PAM-LiCl ionic hydrogels 100 mg and 60% *RH*).

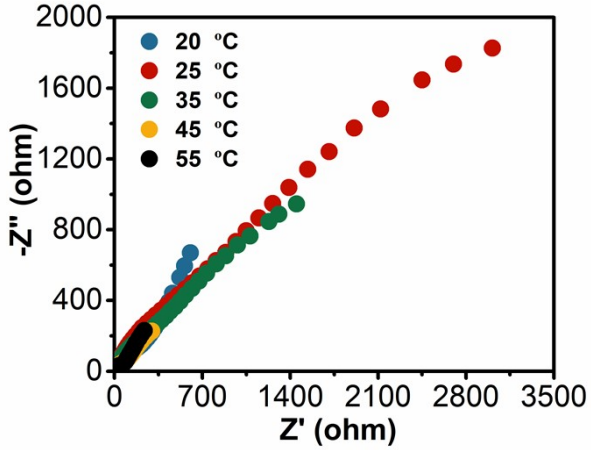

Figure S23 | EIS curves of PAM-LiCl ionic hydrogels at different temperatures and 60% *RH*. Figure 3e is the enlarged part of this Figure.

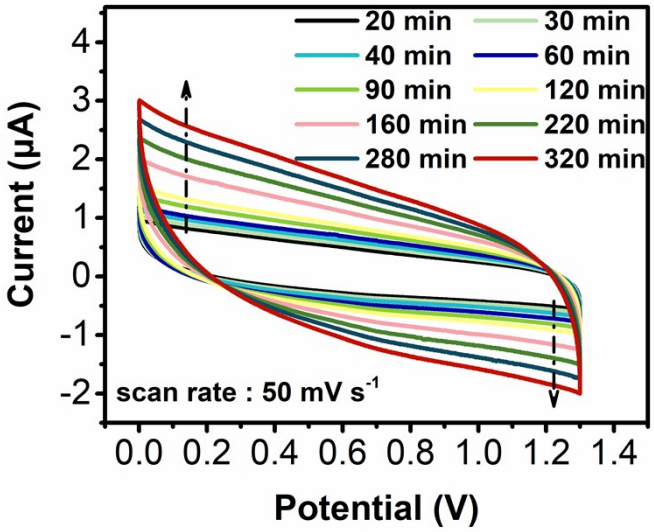

Figure S24 | CV curves of the dry device after exposure to a humid environment for different times at a scan rate of 50 mV s^{-1}.

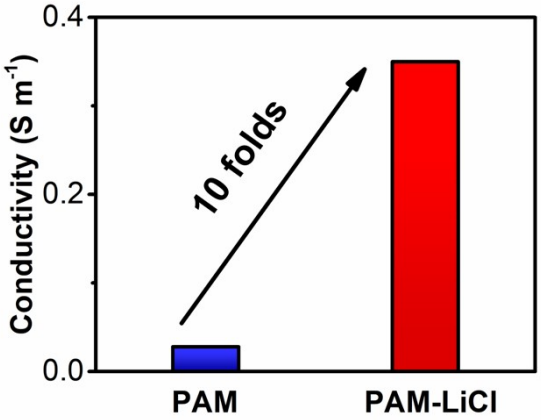

Figure S25 | Ionic conductivities of the PAM hydrogels and PAM-LiCl ionic hydrogels.

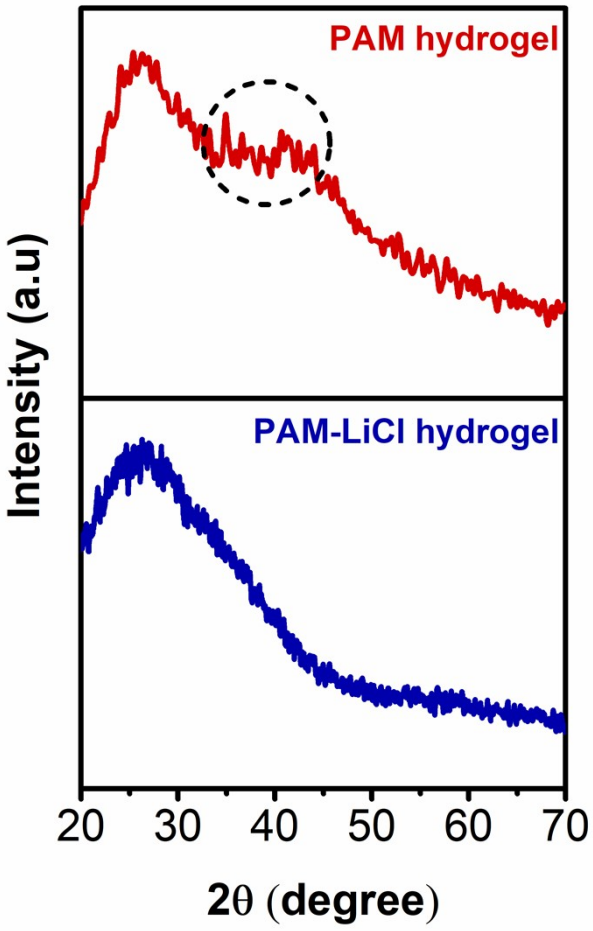

Figure S26 | XRD patterns of PAM hydrogels with and without Li^+ ions.

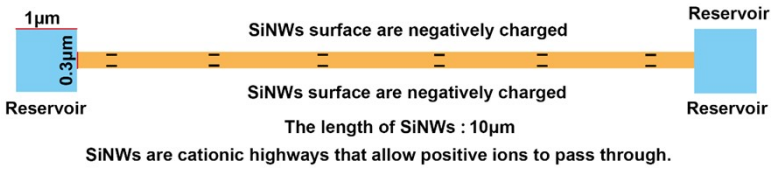

Figure S27 | 2D model for numerical simulation based on PNP theory. The left and right ends are reservoirs (1 μm^2), the center is a simplified nanochannel inside the SiNWs (3 μm^2), and the rightmost end is the surface near the top electrode. Inorganic salt: LiCl (left reservoir Li^+:1×10^{-10}M, Cl^-:1×10^{-10}M; right reservoir Li^+:1×10^{-7}M, Cl^-:1×10^{-7}M); $CaCl_2$ (left reservoir Ca^{2+}:1×10^{-10}M, Cl^-:2×10^{-10}M; right reservoir Ca^{2+}:1×10^{-7}M, Cl^-:2×10^{-7}M); $AlCl_3$ (left reservoir Al^{3+}:1×10^{-10}M, Cl^-:3×10^{-10}M; right reservoir Al^{3+}:1×10^{-7}M, Cl^-:3×10^{-7}M).

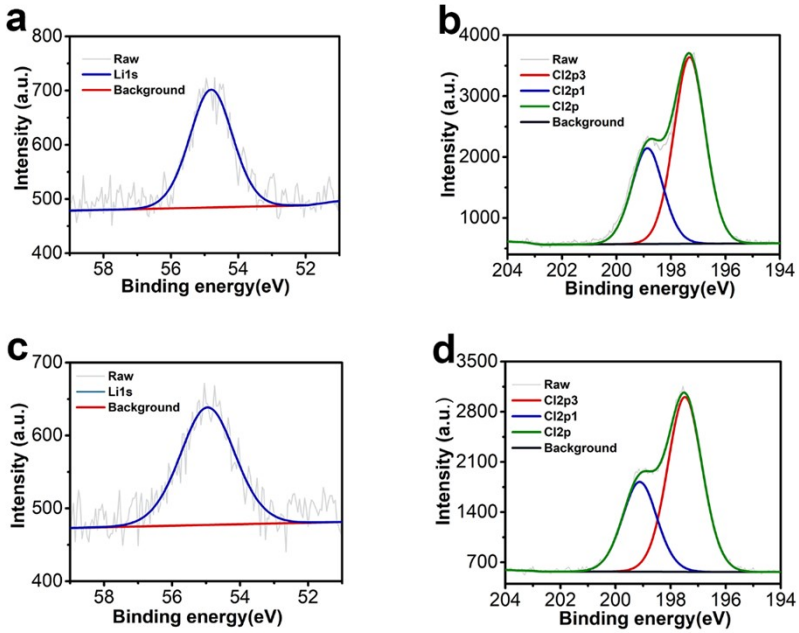

Figure S28 | XPS spectra of PAM-LiCl ionic hydrogels before and after working for one hour. Li 1s spectra (a) before and (b) after work. Cl 2p spectra (c) before and (d) after MEG work.

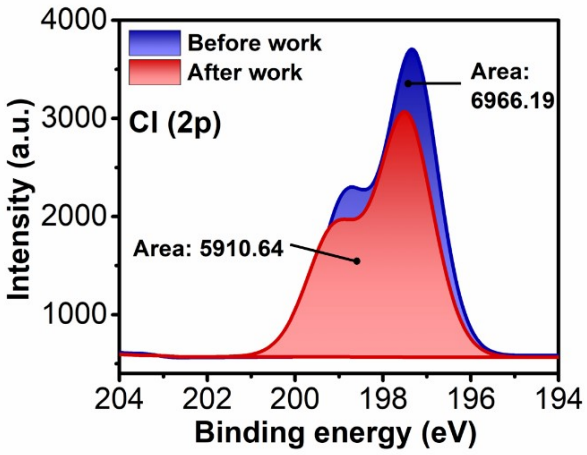

Figure S29 | Cl 2p XPS spectra of the PAM-LiCl ionic hydrogels before and after MEG working for one hour.

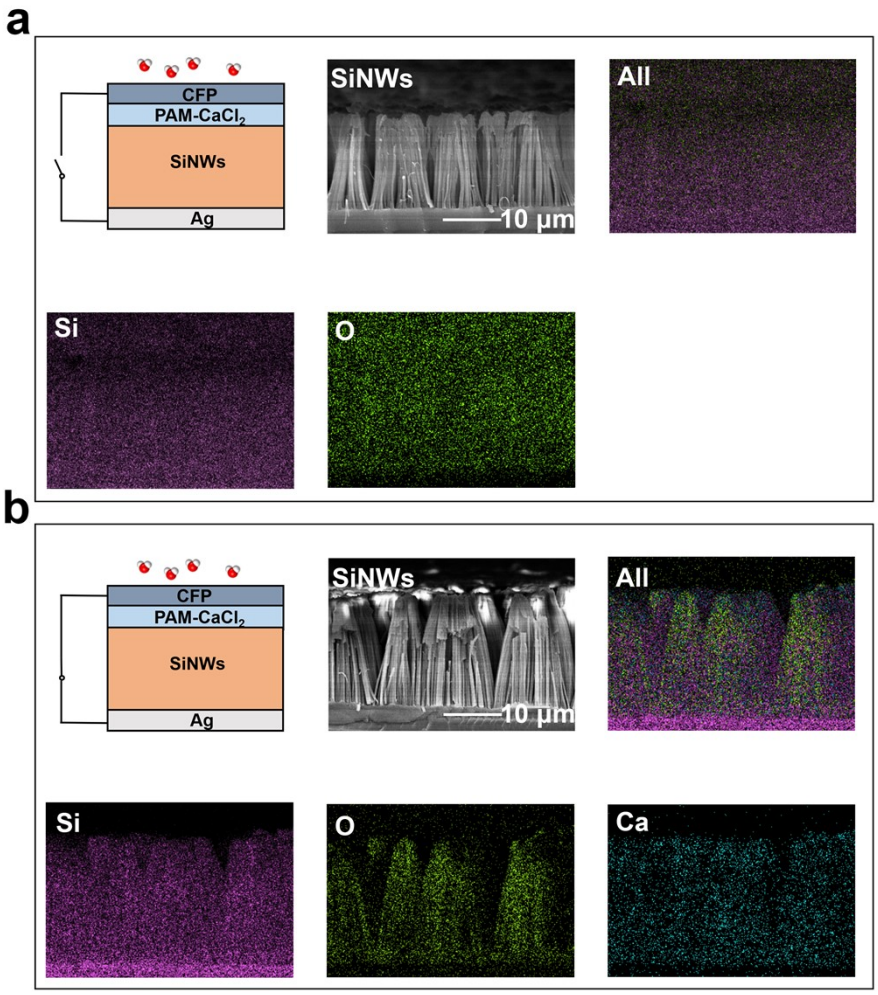

Figure S30 | Comparison of the distribution of elements inside the device before and after work. (a) Element distribution when the device before work. (b) Element distribution after device working for one hour.

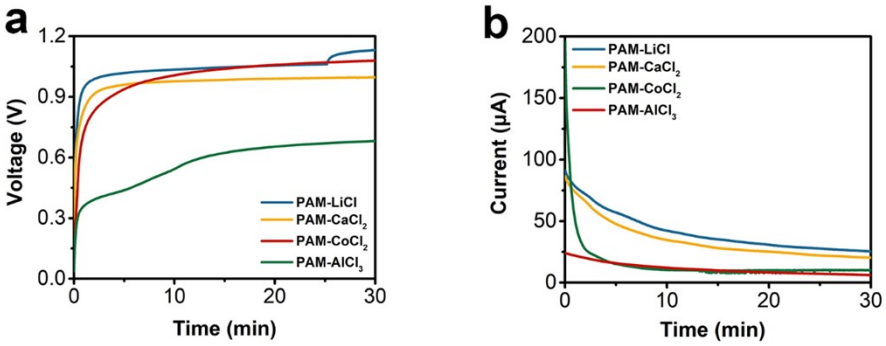

Figure S31 | Constant (a) voltage and (b) current output of hybrid MEGs with different hygroscopic ionic compounds (ionic hydrogels 100 mg, 35 °C and 60% *RH*).

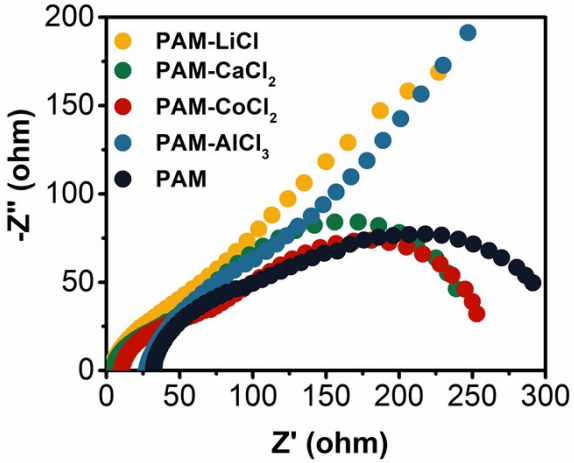

Figure S32 | EIS curve of different hygroscopic ionic compounds. Figure 4f is the enlarged part of this Figure.

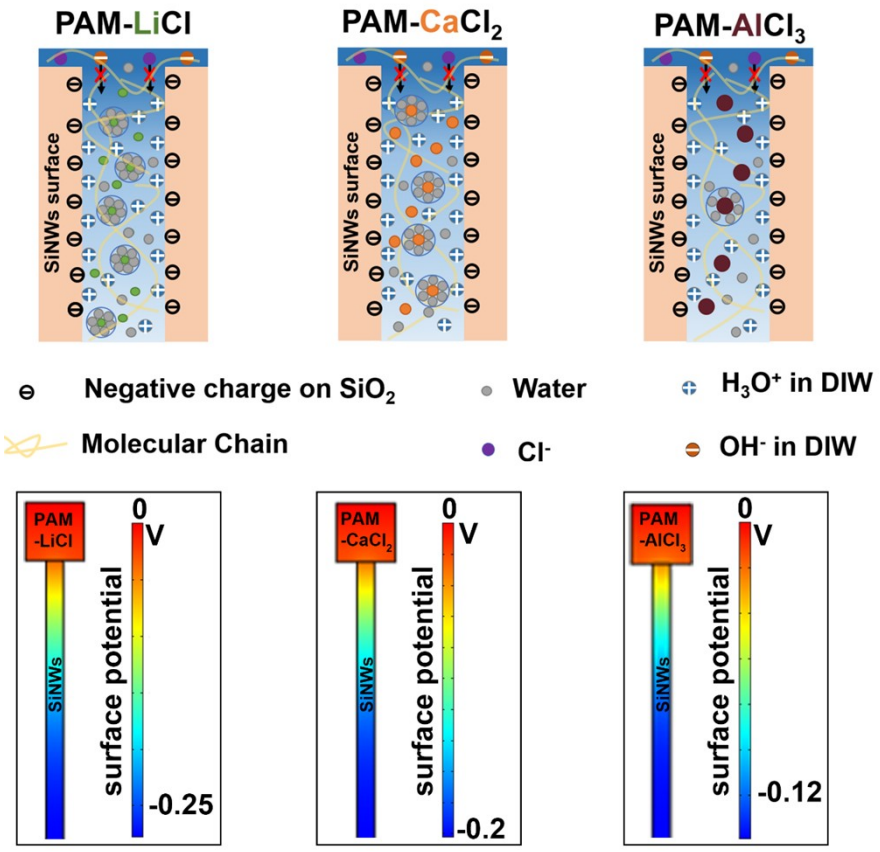

Figure S33 | Schematic representation of the migration of ions with different valence states in SiNWs. As the valence state of ions increase, fewer ions migrate through the SiNWs channel and the migration rate slows down, and the surface potential is also decreasing.

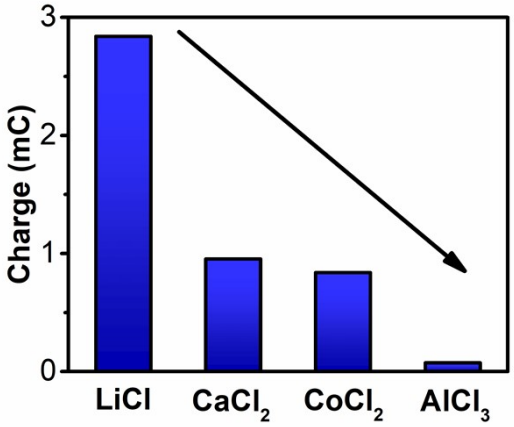

Figure S34 | Produced charges of hygroscopic ionic compounds-MEGs with different metal ions.

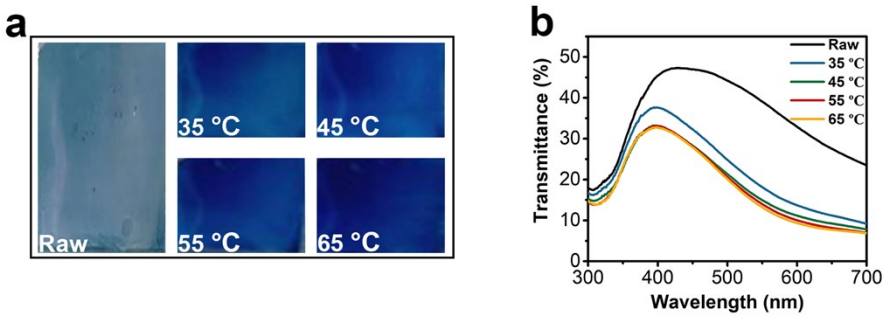

Figure S35 | A single MEG provides power to the electrochromic device at different temperatures and 60% *RH*. (a) At different temperatures, a single device provides power to make electrochromic devices change color to different degrees. (b) The transmittance of a single device that supplies power to an electrochromic device at different temperatures and after electrochromic change.

References

1 H. S. White and A. Bund, *Langmuir*, 2008, **24**, 2212-2218.

2 J. Hao, B. Bao, J. Zhou, Y. Cui, X. Chen, J. Zhou, Y. Zhou and L. Jiang, *Advanced Materials*, 2022, **34**, 2203109.

3 K. Liu, P. Yang, S. Li, J. Li, T. Ding, G. Xue, Q. Chen, G. Feng and J. Zhou, *Angewandte Chemie International Edition*, 2016, **55**, 8003-8007.

4 H. Cheng, Y. Huang, F. Zhao, C. Yang, P. Zhang, L. Jiang, G. Shi and L. Qu, *Energy & Environmental Science*, 2018, **11**, 2839-2845.

5 F. Gong, H. Li, Q. Zhou, M. Wang, W. Wang, Y. Lv, R. Xiao and D. V. Papavassiliou, *Nano Energy*, 2020, **74**, 104922.

6 Q. Lyu, B. Peng, Z. Xie, S. Du, L. Zhang and J. Zhu, *ACS Applied Materials & Interfaces*, 2020, **12**, 57373-57381.

7 M. Li, L. Zong, W. Yang, X. Li, J. You, X. Wu, Z. Li and C. Li, *Advanced Functional Materials*, 2019, **29**, 1901798.

8 Z. Sun, X. Wen, L. Wang, J. Yu and X. Qin, *Energy & Environmental Science*, 2022, **15**, 4584-4591.

9 Y. Zhang, S. Guo, Z. G. Yu, H. Qu, W. Sun, J. Yang, L. Suresh, X. Zhang, J. J. Koh and S. C. Tan, *Advanced Materials*, 2022, **34**, 2201228.

10 F. Zhao, H. Cheng, Z. Zhang, L. Jiang and L. Qu, *Advanced Materials*, 2015, **27**, 4351-4357.

11 Y. Huang, H. Cheng, C. Yang, H. Yao, C. Li and L. Qu, *Energy & Environmental Science*, 2019, **12**, 1848-1856.

12 X. Nie, B. Ji, N. Chen, Y. Liang, Q. Han and L. Qu, *Nano Energy*, 2018, **46**, 297-304.

13 N. Chen, Q. Liu, C. Liu, G. Zhang, J. Jing, C. Shao, Y. Han and L. Qu, *Nano Energy*, 2019, **65**, 104047.

14 Q. Li, Y. Qin, D. Cheng, M. Cheng, H. Zhao, L. Li, S. Qu, J. Tan and J. Ding, *Advanced Functional Materials*, 2023, **33**, 2211013.

15 H. Wang, T. He, X. Hao, Y. Huang, H. Yao, F. Liu, H. Cheng and L. Qu, *Nature Communications*, 2022, **13**, 2524.

16 X. Huangfu, Y. Guo, S. M. Mugo and Q. Zhang, *Small*, 2023, **19**, 2207134.

17 X. Qi, T. Miao, C. Chi, G. Zhang, C. Zhang, Y. Du, M. An, W.-G. Ma and X. Zhang, *Nano Energy*, 2020, **77**, 105096.

18 Y. Qin, Y. Wang, X. Sun, Y. Li, H. Xu, Y. Tan, Y. Li, T. Song and B. Sun, *Angewandte Chemie International Edition*, 2020, **59**, 10619-10625.

19 B. Shao, Z. Song, X. Chen, Y. Wu, Y. Li, C. Song, F. Yang, T. Song, Y. Wang, S.-T. Lee and B. Sun, *ACS Nano*, 2021, **15**, 7472-7481.

20 B. Shao, Y. Wu, X. Chen, Z. Song, Y. Li, Z. Hong, F. Yang, T. Song, Y. Wang and B. Sun, *Advanced Materials Interfaces*, 2021, **8**, 2101213.

21 Y. Wu, B. Shao, Z. Song, Y. Li, Y. Zou, X. Chen, J. Di, T. Song, Y. Wang and B. Sun, *ACS Applied Materials & Interfaces*, 2022, **14**, 19569-19578.

22 Y. Song, Z. Song, C. Jiang, C. Xing, X. Zeng, Z. Zhang, Z. Chen, T. Song, B. Shao, Y. Wang and B. Sun, *Advanced Energy Materials*, 2023, **13**, 2302765.